Ultrasonics - Sonochemistry 43 (2018) 146–155

Contents lists available at ScienceDirect

Ultrasonics - Sonochemistry

journal homepage: www.elsevier.com/locate/ultson

Performance characterisation of a passive cavitation detector optimised for subharmonic periodic shock waves from acoustic cavitation in MHz and sub-MHz ultrasound

Kristoffer Johansen*, Jae Hee Song, Paul Prentice

Cavitation Laboratory, Medical and Industrial Ultrasonics, School of Engineering, University of Glasgow, Glasgow G12 8QQ, United Kingdom

ARTICLE INFO

Keywords:
Passive cavitation detector
Laser-plasma mediated bubbles
Acoustic cavitation
Shock wave
High-speed imaging

ABSTRACT

We describe the design, construction and characterisation of a broadband passive cavitation detector, with the specific aim of detecting low frequency components of periodic shock waves, with high sensitivity. A finite element model is used to guide selection of matching and backing layers for the shock wave passive cavitation detector (swPCD), and the performance is evaluated against a commercially available device. Validation of the model, and characterisation of the swPCD is achieved through experimental detection of laser-plasma bubble collapse shock waves. The final swPCD design is 20 dB more sensitive to the subharmonic component, from acoustic cavitation driven at 220 kHz, than the comparable commercial device. This work may be significant for monitoring cavitation in medical applications, where sensitive detection is critical, and higher frequencies are more readily absorbed by tissue.

1. Introduction

Research involving acoustic cavitation is commonly reported relative to the noise spectrum of the signal collected by a single element passive cavitation detector (PCD), during cavitation occurrence [1–35]. Applications so reported can broadly (but not exhaustively) be categorised as industrial, including sonochemistry [1–7] and cleaning [8–10], and medical therapy[11–29], which may include the use of contrast agent microbubbles to promote cavitation activity [25–29]. Additionally, there is a sizeable volume of literature dedicated to fundamental studies of acoustic cavitation activity, with no particular application stated or investigated, that have incorporated a PCD to record the acoustic emissions [30–35].

In selecting a PCD device to monitor cavitation during an experiment, the researcher has a wide range of options available. Specialist suppliers, such as Sonic Concepts Inc., Precision Acoustics Ltd, and National Physical Laboratory (NPL) offer devices with a stated application as a PCD, supplied with an operating bandwidth, and perhaps the option of some sort of calibration data. Full technical construction details, however, including the active material of the element, are often proprietary [9,11–17,36]. Otherwise, commercially available generic hydrophones, particularly needle [22,29,32,33], and capsule devices [1,23,24] have also been used. Focused lead zirconate titanate (PZT) bowl transducers, that could also be used for transmission, are commonly used in passive receive mode to monitor cavitation activity [6,7,17,20,25]. Bespoke PCDs, developed in-house, are also commonly reported. These are typically constructed from PZT-elements in the form of disks [3,26,31,34,35], or Polyvinylidene fluoride (PVdF) [4,9,26,27].

As varied as the devices that have been utilised as a PCD, are the reporting protocols subsequently used to represent the cavitation measurements recorded, often in an attempt to classify or quantify the activity. PCDs typically exploit cavitation non-linearity, such that measurements are undertaken at frequencies other than the fundamental frequency of the acoustic driving, f_0. Common detection frequencies can be categorised into four groups; subharmonics (f_0/m, where m is an integer value) [1,2,7,10,17,21,24,26,29–32,35], ultraharmonics (nf_0/m, where n is also an integer value, $\neq m$) [1,2,10–13,17,26,27,30–32,36], overharmonics (nf_0) [1,2,7,10–13,17,19,21,24,26,28–32] and broadband noise, sampled from between spectral peaks [1,2,6,10,12,16–19,21,26,30–32,36]. Often, some combination of spectral features are reported, and an inference for stable or inertial cavitation made [2,7,12,21,24,26]. There is, however, an emerging realisation that cavitation activity often exhibits both stable and inertial characteristics, variously referred to as stable-inertial or repetitive transient [37–39]. In contrast to measuring combinations of individual features, the cavitation index quantifies the arithmetic mean power over a certain bandwidth of the spectrum, after the electrical noise has been subtracted [1,23].

* Corresponding author.
E-mail address: k.johansen.1@research.gla.ac.uk (K. Johansen).

https://doi.org/10.1016/j.ultsonch.2018.01.007
Received 30 August 2017; Received in revised form 17 November 2017; Accepted 4 January 2018
Available online 10 January 2018
1350-4177/ © 2018 Published by Elsevier B.V.

For cavitation emission measurements, generally, the benefits of standardisation for the detection and reporting of cavitation activity, and particularly for specific applications, is clear and increasingly recognised [5,27]. Ideally, this would facilitate direct comparison between work published from different groups working on similar applications, however, this is also hindered by a diverse range of experimental exposure configurations. Calibration/characterisation of the PCD used, in any case, is a precursor to any meaningful comparison between studies investigating similar applications. Of the literature sampled above, calibration data – at least at the frequency values monitored – is only sparingly reported [1,3,5,26,32,33]. Moreover, a lack of understanding of the signal emitted by acoustically driven bubbles, has prevented objective analysis of the performance of any given PCD device.

In this paper, we report on the development and characterisation of a PCD based on PVdF. A distinguishing feature of the work is that, from the outset, the device design is targeted at detection of periodic shock waves, and is therefore hereafter referred to as the shock wave PCD (swPCD). Using laser-plasma generated bubble collapse shock waves (BCSWs), and the spectral power distribution within the BCSW, [40], which informed the 'tuning' of the swPCD via backing and matching layers to maximise sensitivity. In Section 2, the rational for swPCD construction, based on a working knowledge of acoustics, is described. Section 3.1 is a description of the experimental arrangement used to test the swPCD, including against a commercially available PVdF-based PCD (Y-107, Sonic Concepts Inc., Bothell, USA). A finite element model supporting shock wave propagation, to verify each construction stage of the swPCD, is also described, Section 3.3. Section 4 presents both swPCD and Y-107 results for the detection of a single BCSW from a laser-plasma mediated bubble, and subharmonic periodic shock waves from a single cavitation cloud, driven by high-intensity focused ultrasound (HIFU).

1.1. The cavitation signal

Clarification of the signal emitted by cavitation is evidently an important consideration for determining the suitability of a PCD for detection of that signal, including any distortions that the PCD characteristics may introduce [40].

We have recently reported high-speed shadowgraphic imaging (described in Section 3.1) of single cavitation clouds, driven by HIFU at fundamental frequencies, f_0 = 254 kHz [35] and 692 kHz [32]. Both reports used laser-nucleation (also described in Section 3.1), to predetermine the instant and location of cavitation inception [34]. The high speed observations indicated that for HIFU driving of pressure amplitudes in the MPa regime, the initial bubble that formed from the nucleation rapidly fragmented into a cloud of closely packed, and strongly interacting component bubbles, within the first few cycles of the resulting cloud. Under subsequent cycles of driving, the component bubbles adopt in-phase oscillations, such that the cloud oscillates at f_0, effectively as a single entity. Strong subharmonic cloud collapses at f_0/m, within the f_0 oscillations and with m increasing for larger driving pressure amplitudes, were observed to be coincident with periodic shock wave emission. In the latter study [32], the combined imaging and acoustic detection of the emitted signal further indicated that periodic shock waves were predominantly responsible for all spectral features recorded at nf_0/m (for all values of n and m), other than ~15 dB of f_0, attributable to scattered driving.

2. Rationale for the swPCD

Taken collectively, these studies indicate that a swPCD designed for sensitivity to lower frequency components of periodic shock waves (and BCSWs, generally), may be expected to offer superior detection of the features commonly reported for cavitation-mediated effects, particularly the subharmonics and their ultraharmonics, but also significant contributions to the overharmonics of f_0.

However, the peak positive pressure amplitude of the shock waves generated by the subharmonic collapses of acoustically driven cavitation clouds are somewhat variable, with clouds of more than a few component bubbles emitting multi-fronted shock waves [32,35]. For the purposes of this report, objective testing of the swPCD is therefore undertaken relative to laser-plasma mediated BCSWs, which have a peak positive pressure amplitude of the shock wave proportional to the maximum radius the bubble attains following the expansion phase [41], through which peak positive pressure amplitude of the shock wave reproducibility may be confirmed.

To demonstrate the utility of identifying the component of the cavitation signal to be detected, as guidance for the design, we compare the performance of the swPCD to a commercially available device, Y-107 from Sonic Concepts Inc (Bothell, WA, USA). Y-107 is constructed to fit within a central 20 mm opening through a HIFU transducer, manufactured by the same company (H-149, Sonic Concepts Inc., Bothell, WA, USA), which we use to drive the acoustic cavitation activity reported below. Y-107 has a 17.5 mm active diameter and is geometrically focused to 68 mm [42], such that it is confocal to the focus of the H-149 HIFU transducer, when *in situ*. It has a stated bandwidth of 10 kHz–15 MHz, and its construction, provided by Sonic Concepts Inc on request, is described as a *"0.2 mm thick piezo-polymer stack, with high acoustic impedance backing material >4 MRayl and an EMI [electromagnetic interference] shielded plastic outer casing (20 mm OD × 40 mm length) to optimize the operating bandwidth and signal-to-noise ratios"*.

The swPCD was therefore designed to be interchangeable with Y-107, within the H-149 HIFU transducer, such that the outer diameter of the 3D printed casing is mm. The casing holds the active material, an unfocused disk of diameter equal to 15mm.

As we are seeking to assess shock wave sensitivity directly (including against a commercially available PVdF-based PCD), PVdF was therefore chosen as the active material for the swPCD. The thickness of PVdF film was selected on the basis of the power spectrum of the BCSW, as described in Johansen et al. [40]. The BCSW power peaks at <1 MHz, it is therefore desirable to select a PVdF-film sensitive to lower frequencies, which can be further tuned with backing and matching layers as outlined Section 3.3.1 and Section 3.3.2, to obtain the largest magnitude subharmonic features. As such, the swPCD is constructed from 110 μm PVdF, as the thickest commonly available film (9–110 μm being commonly available), with the lowest thickness mode resonance frequency of ~10 MHz.

3. Materials and methods

3.1. Experimental setup

The experimental arrangement within which all swPCD testing was undertaken, has been described in detail elsewhere [40,32]. Briefly, a long working distance microscope objective lens (50 × 0.42 NA Mitutoyo Kawasaki Japan) and a HIFU transducer, are arranged within a custom built chamber measuring 420 × 438 × 220mm^3, such that the optical and acoustic foci are aligned, Fig. 1. The chamber has two recessed walls to allow the placement of an imaging optic (Monozoom 7 lens system, Bausch and Lomb, Rochester USA) in closer proximity to the combined foci, and filled with degassed deionized water. Bubble activity, in one of two regimes described below, is imaged with a Shimadzu HPV-X2 (Shimadzu Corp, Kyoto, Japan) high-speed camera, at 1×10^6 frames per second, and with 10 ns synchronous laser pulses (CAVILUX Smart, Cavitar, Tampere, Finland), providing the illumination and shadowgraphic capability for shock wave visualisation.

The HIFU transducer operates at a fundamental frequency of f_0 = 220 kHz and is geometrically focused to 68 mm, with an outer diameter of 110 mm and a 20 mm central hole through the body. The Y-107 PCD is geometrically focused to 68 mm, and designed for insertion

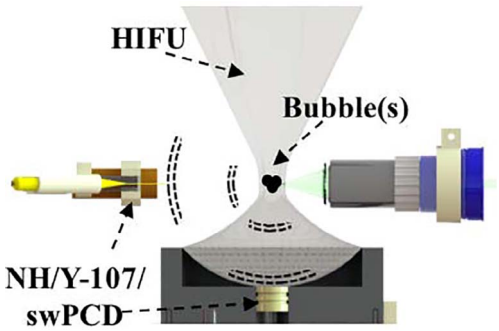

Fig. 1. Experimental setup used for detection of laser plasma-mediated BCSWs (no HIFU), and laser-nucleated acoustic cavitation (with HIFU). Three sensors are depicted, the needle hydrophone, swPCD, and Y-107. The needle hydrophone is used for determining the characteristics of the input function used in the FEM simulation. Needle hydrophone and Y-107 are positioned with an xyz-manipulator. A nucleating laser pulse is focused through the microscope objective lens. swPCD is placed through a hole in a transducer with an O-ring retainer. All sensors are placed at a distance of 68 ± 1 mm from the nucleation site, equal to the geometric focus of the Y-107.

within the hole through the transducer. As mentioned previously, the dimensions of the swPCD were primarily chosen for direct comparison of cavitation measurements recorded with Y-107, and as such the swPCD is also mountable within the transducer. For the various testing described below, the swPCD occupied the hole through the transducer, with Y-107 and the calibrated needle hydrophone (Complex calibration bandwidth is 125 kHz – 20 MHz, 1.0 mm diameter, PVdF, Precision Acoustics, Dorchester, UK) arranged orthogonally to the axis of HIFU propagation, mounted on an xyz-manipulator and positioned 68± 1mm from the bubble activity, Fig. 1.

3.2. Cavitation bubble regimes

Bubble activity is initiated via a single 6–8 ns 532 nm laser pulse (Nano S 130-10 frequency doubled Q-switched Nd:YAG, Litron Lasers, Rugby, UK), represented green Fig. 1, focused through the long working distance objective lens. Two distinct regimes of cavitation activity are reported here, primarily distinguished by the energy of the individual laser pulse; (i) single laser-plasma mediated bubbles and (ii) laser-nucleated acoustic cavitation, which also requires a burst of HIFU simultaneously incident to the combination focal region [34,40]. For the former regime, laser pulses of >4 mJ (determined to be the breakdown threshold for the medium, and the laser focusing optic) generate a plasma and an optical breakdown shock wave, Fig. 12(a) in [32] for example. The plasma rapidly expands to form a comparatively large bubble, of maximum diameter determined by the pulse energy. The inertia of the host medium then deflates and collapses the bubble such that a second shock wave, the BCSW, is emitted. The peak positive pressure amplitude of the BCSW is, in turn, determined by the maximal size of the bubble, which is verifiable through high-speed imaging. In this way, reproducible BCSWs from bubbles of maximum radius $R_{max} = 365 \pm 4\ \mu m$, can be reliably generated to test the effect of adding matching and backing layers to the PVdF-film, during swPCD construction. The BCSWs are also detected with the needle hydrophone, Fig. 1, calibrated for magnitude and phase between 125 kHz–20 MHz (NPL, 2016). Johansen et al. describes the process of deconvolving the impulse response of the needle hydrophone from the voltage trace of the detected shock wave, to restore the pressure waveform, Fig. 7 in [40]. A simulation of the waveform, based on established bubble theory and described fully in [40], serves as an input function for the finite element model, described Section 3.3. Spectra of both the experimentally measured and deconvolved, and the simulated BCSWs are depicted, Fig. 3(b,c), confirming that the lower frequency components of the BCSW contain the highest amplitude components of the shock wave.

For the latter regime, laser-nucleation of acoustic cavitation, a laser pulse of energy below the breakdown threshold (thereby insufficient to generate a plasma), is co-incident to the combined focal region with a burst of 50 cycles HIFU, and serves to nucleate a single cloud of acoustic cavitation. This approach is used to generate controlled acoustic cavitation activity for comparison of the swPCD to Y-107 detection performance Section 4.2, in terms of the periodic shock wave mediated spectral features [32], commonly reported during applications, as described in Section 1.1.

3.3. FEM model of swPCD

Fig. 2(a) is a photograph of the final stage swPCD, with Fig. 2(b) depicting a schematic cross-section, with the components including the PVdF-film, backing and matching layers labeled. Fig. 2(c) is a representation of the finite-element-method (FEM) model of the swPCD, used to verify the effect on the shock wave detection of the device with various matching and backing layer materials. PZFlex (Weidlinger Associates Inc., Glasgow, UK), a commercially available FEM package, used to simulate the acoustic field and propagation effects from a prototyped transducer, was used.

The simulated pressure-time waveform of Fig. 3(b) forms the user-defined input, and planar propagation to the swPCD is modeled. Simulations reported below were undertaken at a meshing frequency of 40 MHz, with convergence confirmed for 50 and 60 MHz, with 16 elements per wavelength. Rotational symmetry around the axis, Fig. 2(c), reduces computational load and mimics 3-dimensional effects.

3.3.1. Backing layer

Backing materials are used to 'tune' the characteristics of a

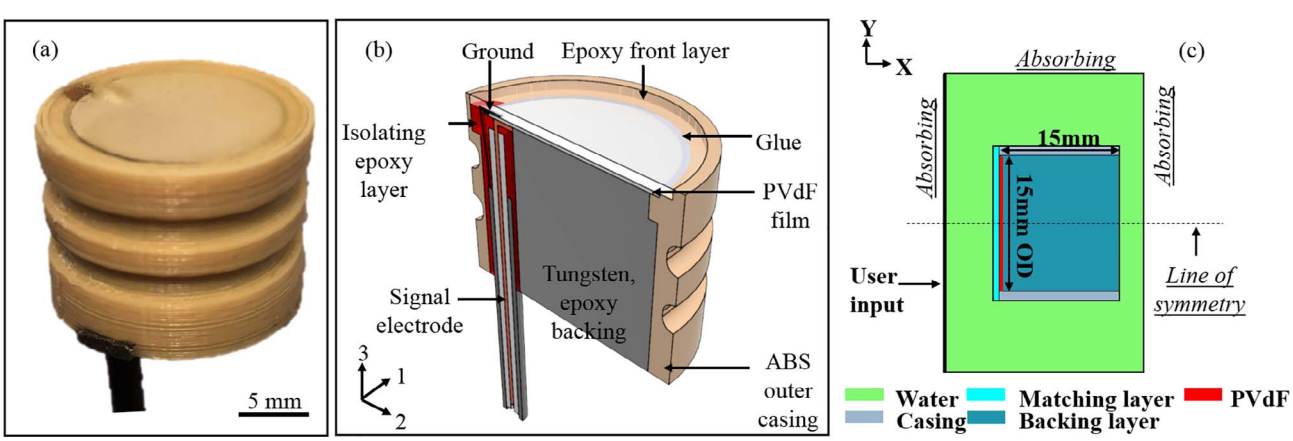

Fig. 2. (a) Final stage swPCD, (b) schematic cross-section of the swPCD, and (c) schematic of FEM geometry used in the guidance of swPCD construction.

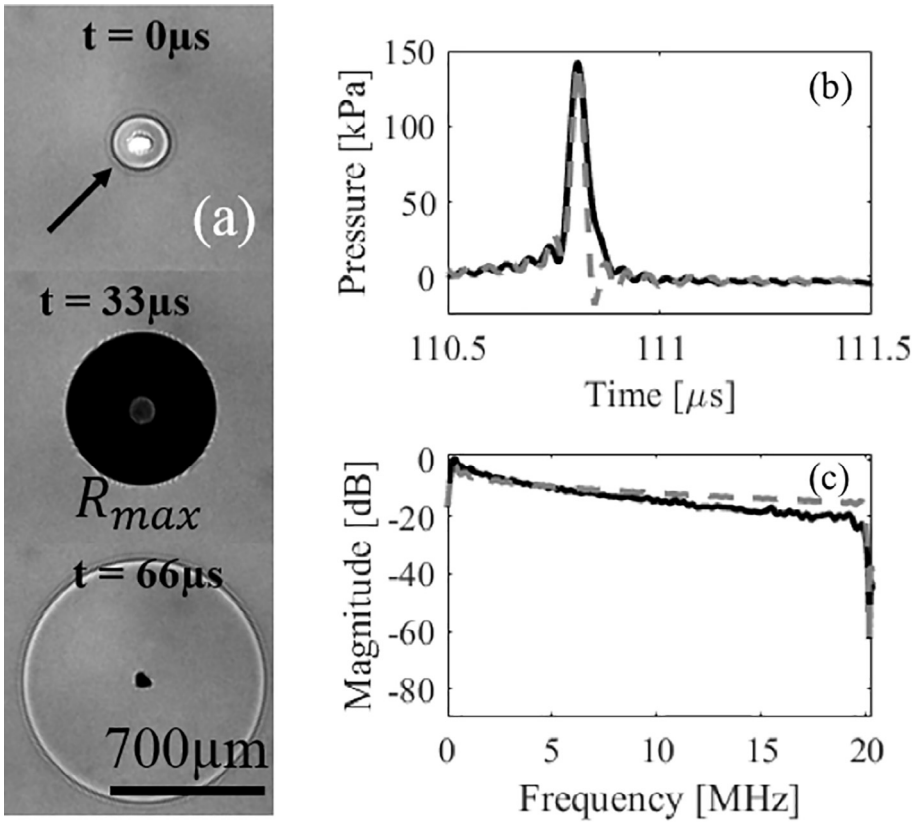

Fig. 3. (a) High-speed shadowgrapic images of the key stages for a laser plasma-mediated bubble, including plasma and OBSW generation, maximum radius, $t = 33\,\mu s$, and collapse with coincident emission of a BCSW at $t = 66\,\mu s$, imaged at 1×10^6 frames per second. The peak positive pressure amplitude of the BCSW is intrinsically related to R_{max} (b) Full waveform deconvolved BCSW (solid black) measured by needle hydrophone from laser plasma-mediated bubble at a distance of 68 mm, and computed BCSW (stapled gray) bandpass filtered at 125 kHz–20 MHz. (c) Spectra of experimentally detected and computed BCSW, where the computed BCSW spectra is normalised to the maximum of the experimentally detected BCSW.

piezoelectric material, promoting narrow-band or broadband features [43–45]. For the swPCD, heavy backing, such as epoxy loaded with tungsten powder, is used to promote broadband characteristics. Moreover, if the backing is of acoustic impedance higher than the active material, then $\lambda/4$ resonance behavior can be expected [46], this advantageously shifts the resonance frequency down towards the low components in periodic shock waves. Representative results from the FEM investigation of backing layers for the swPCD are shown in Fig. 4, with both (a) the time waveform representation of the detection of a BCSW, and (b) the relative sensitivity deconvolved from the BCSW spectrum over the needle hydrophone calibration bandwidth. The pertinent properties for the materials presented are given in Table 1.

In order to suppress reflected shock wave detection within the swPCD, a 15 mm thick backing layer, at attenuation 3.43 dB/(cm × MHz), was deemed sufficient.

FEM simulation allows for assessment of air and 25% volume fraction (VF) Tungsten-Epoxy as indicative of the effects for low and high acoustic impedance backing respectively, relative to unbacked (or water backed) PVdF-film. Fig. 4(b) confirms that the unbacked PVdF-film has a $\lambda/2$ thickness resonance around ~ 10 MHz. This feature is enhanced by air backing, which also decreased sensitivity for frequencies below 2 MHz. In contrast, 25% VF Tungsten-Epoxy promotes $\lambda/4$ thickness resonance. Specifically, there is a ~ 4 dB increased relative sensitivity for frequencies below 6MHz. As discussed in Section 1.1, and represented in Fig. 3(c), this is the bandwidth of the BCSW containing the highest pressure amplitudes.

The results discussed for Fig. 4(b) manifest the following way in the time-domain, Fig. 4(a). For air backing, the peak-normalised output is decreased by 27%, and both the rise-time (RT)[32] and the full-width-half-maximum (FWHM) are decreased, compared to the unbacked swPCD. Conversely, for the 25% VF Tungsten-Epoxy, the peak-normalised output is increased by 44%, and both the RT and the FWHM are increased. The non-smooth response seen for both the unbacked and air backed swPCD, are due to reflections between the PVdF and backing layer, which would manifest in the impulse response of the swPCD. These reflections are also representative examples of detector convolution artifacts, which can all be removed by deconvolving the detected signal with the complex impulse response to the detector [40].

3.3.2. Matching layer

Matching layers are designed to increase the transmission coefficient around resonance [44]. This is ultimately making the transducer more broad-band, with a higher absolute sensitivity within the operation bandwidth. If a single matching layer is to be used, quarter-wavelength thickness of the centre frequency is ideal [47,48]. PVdF-based transducers, including PCDs, are generally not matched, as it is counterproductive to match a material for a single centre frequency, considering this active material is generally selected on account of its broadband properties. However, the swPCD is matched to target the subharmonic features in the cavitation spectrum. For this work the following equation was used to approximate the optimal acoustic impedance of a single matching layer, Z_{ml} [47].

$$Z_{ml} = \sqrt{Z_W Z_{PVdF}} \tag{1}$$

where Z_W, and Z_{PVdF} are the acoustic impedance of water and PVdF, respectively.

The FEM investigation of matching layers for the swPCD are shown in Fig. 5, with both (a) the time-domain representation of the detection of a BCSW, and (b) the relative sensitivity. The pertinent properties for the materials presented, are given in Table 2.

Two representative results from the investigation of matching layers materials are presented, in addition to unmatched (PVdF-film backed by 25% VF Tungsten-Epoxy); both of which are close to the optimal acoustic impedance computed from Eq. 1, of ~ 2.62 MRayl. The inset of Fig. 5(b), indicates that the swPCD matched with both materials, at a layer thickness of 1 mm, have a higher relative sensitivity from ~100–900 kHz, compared to the unmatched swPCD design. Furthermore, at higher frequencies (>4 MHz) the presence of a matching layer

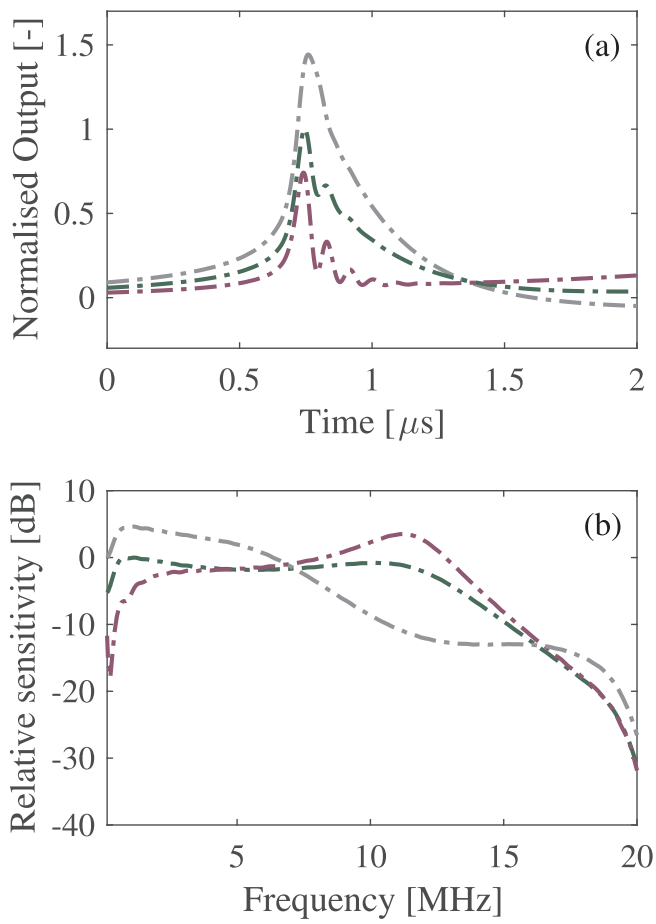

Fig. 4. (a) FEM simulation of BCSW detection using air backing (violet) and 25% Tungsten-Epoxy (grey) backing layers, as representatives of low and high acoustic impedance respectively. Results are normalised to PVdF-only (green) as no backing (or water backing). (b) Relative sensitivity for the backing configurations investigated in (a). (For interpretation of the references to colour in this figure legend, the reader is referred to the web version of this article.)

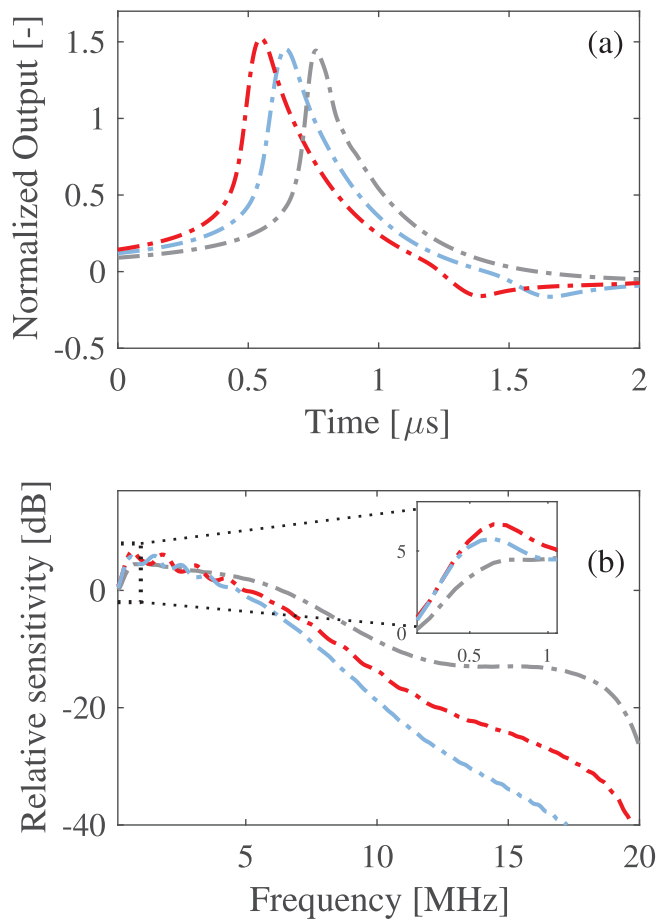

Fig. 5. (a) FEM simulation of BCSW detection using epoxy materials Vantico HY956EN/CY208 (light blue) and Vantico HY956EN/CY221(red) as matching layers, representatives of close to desired acoustic impedance respectively. All results have a backing layer of 25% Tungsten-Epoxy (red) and normalised to PVdF-only (water backing), 4. (b) Relative sensitivity for the backing configurations investigated in (a). (For interpretation of the references to colour in this figure legend, the reader is referred to the web version of this article.)

Table 1
Material properties of backing layer investigated using FEM. Attenuation and longitudinal speed of sound are measured at 1 MHz, taken from the PZFlex database.

Material	Density [kg m^{-3}]	Longitudinal. velocity [ms^{-1}]	Impedance [MRayl]	Attenuation [dB cm^{-1} MHz^{-1}]
Air	1.24	343	0.000425	1.64
Water	1000	1500	1.50	0.0022
25% VF tungsten/epoxy	5710	1750	9.99	3.43

Table 2
Material properties of matching layer investigated using FEM. Attenuation and longitudinal speed of sound are measured at 1 MHz, taken from the PZFlex database.

Material	Density [kg m^{-3}]	Longitudinal velocity [ms^{-1}]	Impedance [MRayl]	Attenuation [dB cm^{-1} MHz^{-1}]
Water	1000	1500	1.50	0.0022
Vantico HY956EN/CY208	1165	1989	2.31	16.33
Vantico HY956EN/CY221	1134	2452	2.78	8.95

decreases the relative sensitivity of the high frequency content.

The results discussed for Fig. 5(b) manifest the following way in the time-domain, Fig. 5(a). The two different matching materials suggest that a 8–13% gain in peak-normalised output can be achieved by tuning the performance of the swPCD with a matching layer, in which an identical argument as presented for the heavy backing, holds true for this increase. Moreover, as the speed of sound is higher in the matching layers, compared to water, the BCSW arrives earlier at the PVdF-film, combined with a reflection of BCSW within the swPCD, displayed as a negative phase in the normalised output, 5(a). Equivalently, as for the results presented in Fig. 4(a), these reflections are representative examples of detector convolution artifacts, which can be removed by deconvolving the detected signal with the complex impulse response to the detector[40].

A summary of all the component materials selected for the swPCD, with material properties is seen in Table 3

4. Results

The results sections below are arranged as follows; Section 4.1.1 demonstrates qualitative agreement for BCSW detection between the FEM and experimental approaches, for each stage of swPCD construction, specifically the addition of backing and matching layers to the PVdF-film. Section 4.1.2 presents simultaneous detection of BCSWs for the final stage swPCD, and the Y-107 PCD, along with a description of the detectors' relative sensitivities. Section 4.2 validates the design and

Table 3
Material properties of final swPCD taken from PZFlex database.

Material	Density [kg m^{-3}]	Longitudinal velocity [ms^{-1}]	Impedance [MRayl]
Water	1000	1500	1.50
HY956EN/CY221	1134	2452	2.78
110 μm PVdF	1780	2560	4.56
25% VF tungsten/epoxy	5710	1750	9.99

testing of the swPCD, through the detection of a single laser-nucleated acoustic cavitation cloud, resolved by high-speed shadowgraphic imaging, and emitting low pressure amplitude periodic shock waves [32]. These results are presented in parallel with simultaneous measurements taken with the Y-107 PCD, from the same cavitation cloud, and a comparison between both PCD performances is made.

4.1. Detection of a single laser plasma mediated BCSW

4.1.1. For each swPCD construction stage

Fig. 6 (a) presents measurements taken of laser plasma-mediated BCSWs of comparable maximum diameter, verified via high speed imaging, for each stage of swPCD construction at a distance of ~ 68 ± 1mm from the plasma position. The measurements confirm that the FEM predictions of Section 3.3.1 and Section 3.3.2 translate to the performance of the physical swPCD, in terms of peak-voltage output, RT and FWHM. The discrepancies between the experimental measurements and the FEM simulations can in part be explained by the assumption of a plane wave in the simulation, experimentally some spatial-averaging would be expected from a spherically diverging BCSW. In addition, the input BCSW has a slight overestimation of the high frequency content, Fig. 3(c), which combined with the plane wave assumption contributes to the shorter RT and FWHM, Table 4. Fig. 6 (b) depicts the spectra for the experimental measurements, again confirming the effect on the sensitivity of the backing and matching layers. The noise floor for each swPCD construction stage, assessed from the voltage output prior to BCSW detection, is also presented. The salient features of Fig. 6 (b) are the ~ 4–5 dB increase in sensitivity <2MHz on the addition of the Tungsten-Epoxy backing layer, and the ~ 1 dB increase on the addition of the CY221 matching layer for between 0.1 and 0.6 MHz. Conversely, for the higher frequency components, the backed and matched swPCD converges with the noise floor at ~ 7.0 MHz.

Table 4
Summary of normalized amplitude, RT and FWHM for both experimental and computational results for all build stages of the swPCD. All results are normalised to PVdF-film only.

swPCD	Norm. Amp. Exp./Sim.	RT [ns] Exp./Sim.	FWHM [ns] Exp./Sim.
PVdF-film only	1/1	375/408	265/185
With backing	1.53/1.44	620/447	390/228
With matching and backing	1.56/1.52	635/483	415/268

4.1.2. The swPCD versus the Y-107 PCD

Fig. 7 represents experimental measurements taken of the same BCSW with the final stage swPCD and the commercial Y-107 PCD, with the devices at 68 ± 1 mm (geometric focus to Y-107) from the plasma location in the configuration of Fig. 1, in (a) the time-domain and (b) the frequency-domain (with noise floors for each, as described previously). Fig. 7 (a) indicates that the peak-voltage output from the swPCD is ~ 4× that of Y-107, with a RT and FWHM ~ 6×longer. Fig. 7 (b) reveals that these features are readily explained by an dB greater magnitude response at ~ 1MHz, and an −10 dB at 7 MHz difference in the magnitude response of the PCDs. In terms of signal-to-noise ratio (SNR), the swPCD exhibits 40–60 dB across the frequencies <2 MHz, compared to the Y-107 20–30 dB.

4.2. swPCD and Y-107 detection of acoustic cavitation

The previous results sections dealt with testing and characterization of the swPCD (and Y-107 PCD) against laser-plasma mediated BCSWs, as a verifiable and reproducible shock wave source. In this section, the energy of the laser pulse is reduced to below the breakdown threshold for the host medium and laser focusing arrangement, and a burst of HIFU generated to be incident simultaneously to the combined laser-HIFU foci. This serves to generate a single acoustic cavitation cloud at a predetermined position and instant, such that the PCDs can be configured to detect the activity and the detections meaningfully compared, and the bubble activity itself resolved with high-speed shadowgraphic imaging.

Fig. 8(a) is representative high-speed images of a cavitation cloud, driven by HIFU at f_0 = 220 kHz and peak-pressure amplitude equal to 682.9 ± 62.0 kPa, with the Q-switch of the laser taken as t = 0 μs. The imaging confirms the cloud undergoes f_0 oscillations, with strong

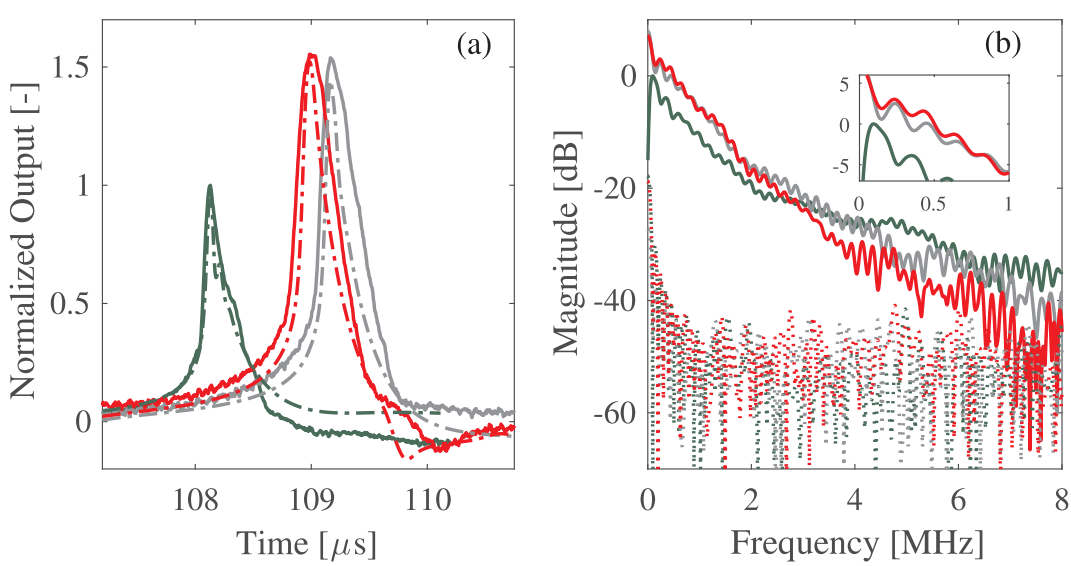

Fig. 6. Comparison of experimentally detected (solid) and simulated BCSW (dashed) response for different construction stages of swPCD. For PVdF-only (green),backed PVdF (gray), matched and backed (red). All measurements are performed at ~ 68 ± 1mm from nucleation site, where all laser plasma-mediated bubbles had a maximum radius of 365 ± 4 μm. (b) Spectra of shock waves detected by different build stages. Same color coding as in (a), with dotted spectra representing the noise floor for the different stages. All experimental and simulated results are normalized to PVdF-only. (For interpretation of the references to colour in this figure legend, the reader is referred to the web version of this article.)

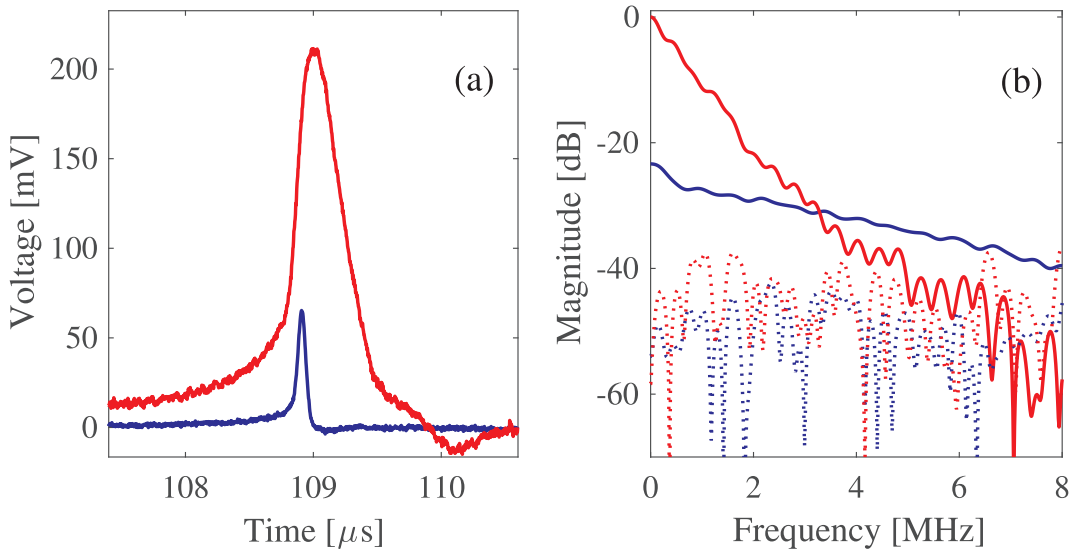

Fig. 7. (a) Voltage-trace comparing final stage swPCD (solid red) and Y-107 (solid blue) for detection of a BCSW. (b) Spectra of shock waves in (a), where stapled data represents the noise floor. Spectra are normalized to final stage swPCD. (For interpretation of the references to colour in this figure legend, the reader is referred to the web version of this article.)

collapses and periodic shock wave emission at $f_0/2$, with periodic shock waves arrowed in (a) at 106 μs, 124 μs and 179 μs, consistent with what we have reported previously [32,33,35].

Fig. 8 is the time waveform and frequency spectra data from (b,d) the swPCD and (c,e) the Y-107, from detection of the cloud represented in Fig. 8(a). The periodic shock waves arrowed in the imaging data are

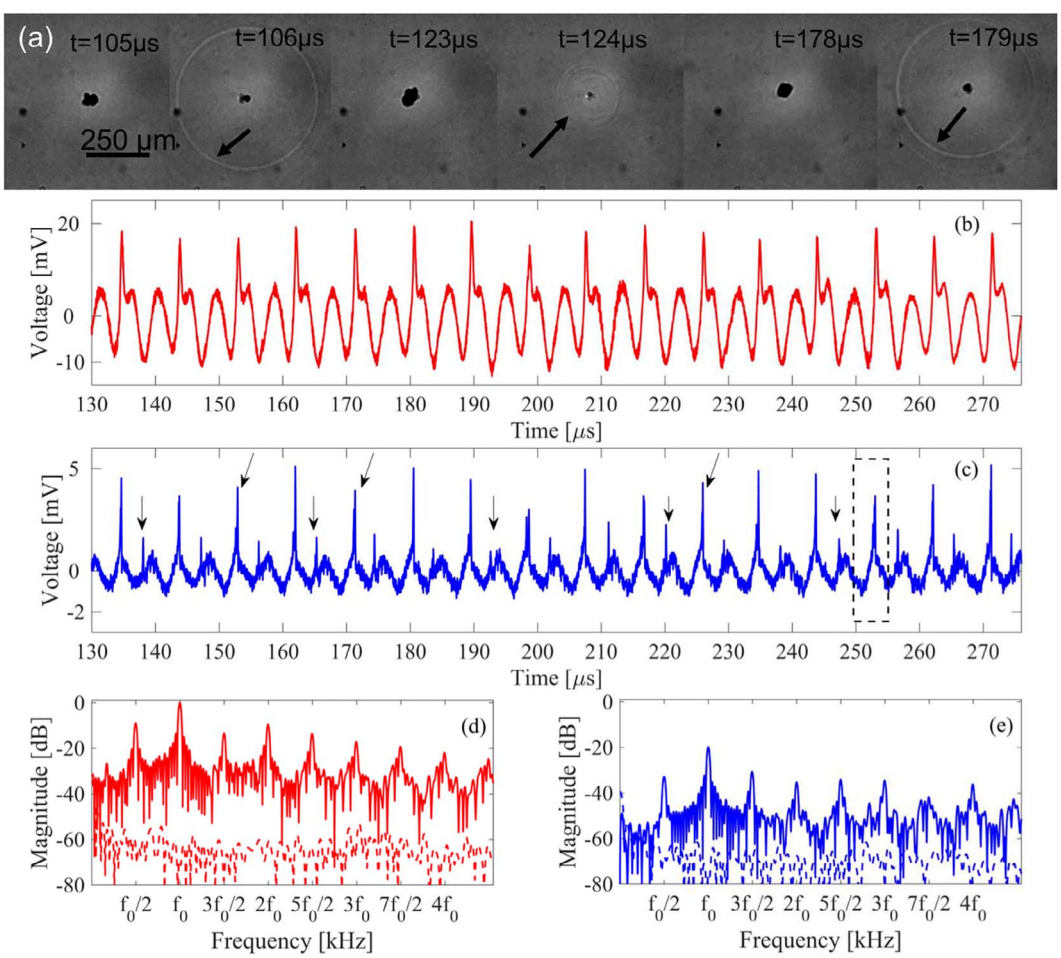

Fig. 8. (a) High-speed shadowgraphic images of subharmonically collapsing cavitation cloud imaged at 1×10^6 frames per-second. (b,c) Control subtracted cavitation emission data in the time-domain detected by (b) swPCD and (c) Y-107. (d,e) Spectra of data in (b,c), where swPCD (solid red) with noise-floor (stapled red), and Y-107 (solid blue) with noise-floor (stapled blue). All spectra are normalized to the maximum of swPCD, with f_0 = 220 kHz. (For interpretation of the references to colour in this figure legend, the reader is referred to the web version of this article.)

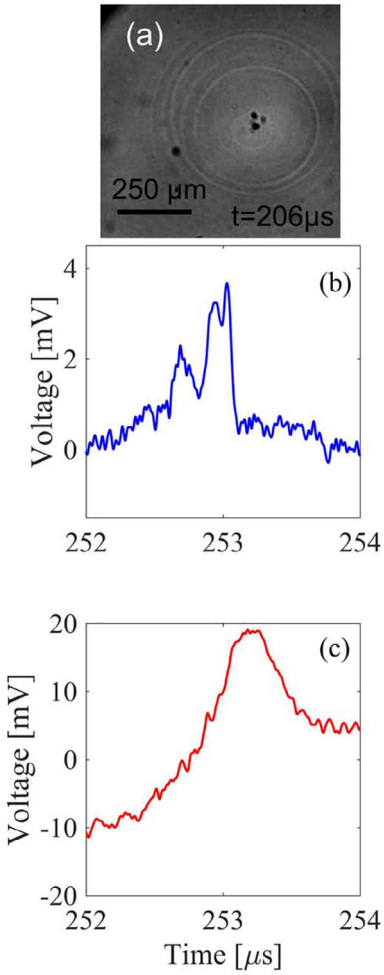

Fig. 9. (a) High-speed image of multi-fronted periodic shock waves from asymmetric cavitation cloud collapse imaged at 1×10^6frames per second. Cavitation emission data subtracted control during detection of multi-fronted periodic shock waves, detected by (b) Y-107 and (c) swPCD

similarly arrowed (angled) in the acoustic data for Y-107. A control exposure, whereby HIFU is generated but no cavitation is laser-nucleated has been subtracted in each case, such that the data represents the cavitation emission signal only, as detected by each detector at 68 ± 1mm.

Inspection of the time-domain data from each PCD indicates that the periodic shock waves within the emission signal detected by the swPCD are ~ 4× the voltage-output of those detected by Y-107 (note different voltage scales), consistent with the plasma-mediated BCSW detection result of Section 4.1.2. Accordingly, from the spectra of the emission signal detected by each PCD, the magnitude of the $f_0/2$ subharmonic peak is dB higher for the swPCD than for the Y-107. Moreover the swPCD has an SNR of ~ 50 dB, compared to Y-107 of dB, at this frequency value.

As described previously, Section 1.1, larger cavitation clouds that have developed in higher pressure amplitude HIFU exposures, collapse non-uniformly, such that periodic shock waves are often multi-fronted with up to 10's of ns between the component fronts. An example of such an emission from the cavitation cloud of Fig. 8, is highlighted in Fig. 9, along with the voltage-time domain data collected with each PCD device. Fig. 9 (b) demonstrates that Y-107 distinguished the component periodic shock wave fronts, whereas the swPCD, Fig. 9 (c), did not. Whilst Y-107 if geometrically focused, such that the spherically radiating shock-fronts will have better planar incidence on the detecting surface, the inferior sensitivity at higher frequencies of the swPCD, identified in Fig. 6(b) also limits the temporal resolution. We finally note the detection of reflected periodic shock waves in the data collected by Y-107, Fig. 8 (c) arrowed vertically. These are reflections from the lens-casing, Fig. 1, which introduces a spectral windowing effect, that is fully assessed in Appendix A.

5. Discussion

In this report, we provide a comprehensive performance evaluation for a simple, inexpensive and easy-to-fabricate PCD design. Identification of a specific component within the cavitation emission signal - periodic shock waves, which have recently been shown to make significant contributions to many non-linear spectral features [32] – allowed optimisation of the swPCD for detection of high power, low frequency components within the individual BCSWs [40]. This was primarily realised through the rudimentary use of a high acoustic impedance Tungsten-Epoxy (>10 MRayl) backing layer to adjust the resonance of 110 μm PVdF film (~ 4.56 MRayl), toward sensitivity for the target bandwidth (<5 MHz).

The utility of identification of the target signal component, and subsequent design of the swPCD, is demonstrated via coincident detection of controlled and resolved cavitation activity relative to a commercially available PCD device, with the dimensions and the active material of the swPCD selected to permit the comparison. The swPCD exhibited a ~ 30 dB higher SNR than the commercial device at $f_0/2$ (f_0 = 220 kHz), and superior sensitivity up to ~ 3 MHz. This bandwidth covers many commonly reported cavitation emission frequencies, in sub-MHz and MHz ultrasound, as well as for higher values of f_0 driving. We note that the swPCD design effectively sacrifices temporal resolution for magnitude sensitivity, although a geometrically focused swPCD may be expected to improve the temporal resolution, and indeed further improve sensitivity via a closer approximation to planar incidence. Moreover, the large active area of the device will endow the swPCD with poor directivity, which was necessary for the comparison to Y-107. We would therefore advocate swPCD dimensions tailored to the experimental requirements within which it is to be deployed.

More generally, we would suggest that improved characterisation of PCDs in the literature is essential; to facilitate better comparison of reports on cavitation mediated effects, with magnitude calibration at the stated frequencies as a minimum requirement. For cavitation emission signals within which shock wave content plays a significant role, however, an assessment of impulse response is also highly desirable. This would typically require expensive and often time-consuming calibration procedure at a national institute with accredited and standardised instrumentation.

Although appropriate characterisation is a prerequisite to good cavitation reporting, we recognise that there are other obstacles to fully and transparently communicating single element PCD detection of cavitation, such as the reflection-induced spectral windowing identified and described in Appendix A. Although reflected periodic shock waves had a marginal influence of ~ 2.4dB on the comparison of the swPCD to the Y-107 performance, two or more 'apparent' cavitation sources (either actual sources, or reflecting objects) can corrupt any reporting that assesses emissions based on the magnitudes of spectral features, and potentially significantly suppress those features such that they become obscured from the spectrum. An assessment of reflection-effects around the expected cavitation location, and the location of the PCD within a given experimental configuration, is recommended.

6. Conclusion

A bespoke PCD design is described, targeting periodic shock wave content within acoustic cavitation emissions. We demonstrate rapid-prototyping of the swPCD in a FEM package can be used for guidance on optimal backing and matching layers. Experimental characterisation was conducted using laser-plasma mediated bubbles, which provided reproducible BCSWs for testing of each construction stage. The final stage swPCD outperforms a comparable commercial PCD by dB at the $f_0/2$ subharmonic. Appropriate characterisation, at stated detection

frequencies, and an assessment of impulse response, is required for PCD reporting and quantification of bubble activity. The role of reflections, and spectral peak suppression are also discussed with regards to cavitation reporting.

Acknowledgments

The research leading to these results has received funding from the European Research Council under the European Union's Seventh Framework Programme (FP/2007-2013)/ERC Grant Agreement No. 336189 (TheraCav). The authors also acknowledge Miriam Jiménez García, Dr. Keith Johnston and Kenneth Kirkeng Andersen for constructive discussions and technical assistance. We are also grateful to PZFlex for significant input to the validation models, and Andrew Tweedie in particular.

Appendix A. Spectral peak suppression from reflections

In this appendix, we draw attention to the minor (vertically arrowed) peaks in the Y-107 time-domain data, Fig. 8 (c). These are periodic shock wave reflections from the laser focusing objective lens casing, Fig. 1, and may be expected to introduce a spectral windowing effect, such as that we have recently described for multiple spatially configured nucleations [33]. The windowing for this particular case is assessed in Appendix A, where it is shown to have a ~ 2.4 dB reduction of the magnitude of the subharmonic peak detected, by the Y-107 PCD.

As reviewed in Section 1.1, we have recently described the role of subharmonic periodic shock waves emitted by cavitation clouds, such as presented in Fig. 8, in the cavitation noise spectrum [32]. We subsequently demonstrated that more than one cavitation event occurring simultaneously, presenting as multiple sources of periodic shock waves, can significantly affect the spectrum detected by a single element PCD [33]. In the specific example presented in [33], two cavitation bubbles emitting $f_0/2$ periodic shock waves, configured as ~ 1λ apart in 692 kHz focused ultrasound, with respect to the tip of the needle hydrophone used in the current work, (which acted as a PCD in [33]), generate shock waves that are incident to the tip with an apparent frequency of f_0. This significantly suppresses the subharmonic features in the spectrum of the combined emissions, despite both bubble sources responding in the $f_0/2$ regime. In [33], a simple expression is derived for assessing the 'spectral windowing' for this, and other spatial configurations of multiple simultaneous cavitation events, in terms of the periodic shock waves detected by the PCD from each source. The derivation relies on synthetic reconstruction of the emitted signal [32], using simulated BCSW profiles, in the time domain.

The periodic shock waves from the acoustic cavitation activity detected by Y-107, Section 4.2, are detected in combination with the periodic shock wave reflections from the laser-focusing lens casing (arrowed Fig. 8 (c)), as may be anticipated from the experimental arrangement of Fig. 1. The combination of directly detected and reflected detected periodic shock waves should therefore be expected to introduce some windowing effect to the spectrum of Fig. 10, which will have enhanced or suppressed the various spectral features, as presented.

For objective comparison of the relative performances of Y-107 and the swPCD at $f_0/2$, the spectral suppression must therefore be assessed. The spectral windowing function that applies to the spectrum of a series of directly detected periodic shock waves, $x_{\mathrm{Dir}}(t)$, by the concurrent detection of a series of reflected periodic shock waves, $x_{\mathrm{Ref}}(t)$, may be approximated by:

$$x_{\mathrm{Ref}}(t) \approx r\, x_{\mathrm{Dir}}(t-\tau) \tag{A1}$$

Where r is the ratio of the average peak positive pressure amplitude of the reflected periodic shock waves to those detected directly, and τ the difference in detection time. The window function that may be expected to be imposed over the spectrum of the combined directly detected and reflected periodic shock waves, as detected by Y-107, may be further approximated by

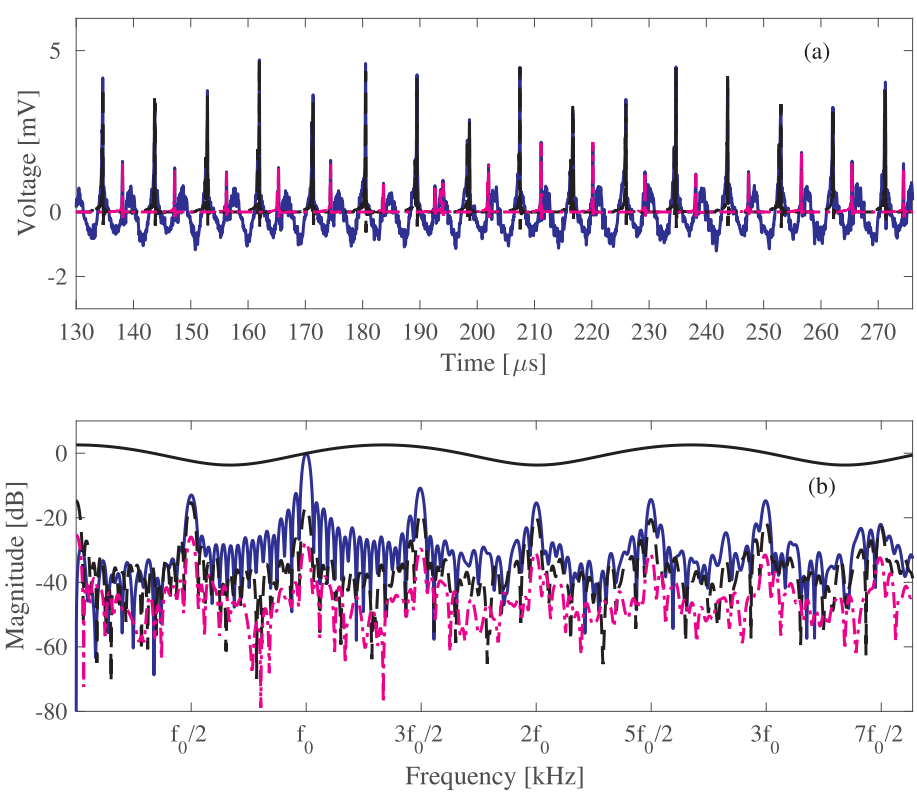

Fig. 10. (a) voltage-trace of Y-107 (blue), synthetically reconstructed direct acoustic emission (stapled black), and synthetically reconstructed reflected acoustic emission (dotted magenta). (b) Spectra of all time domain signals in (a), and spectral window (solid black) imposed on the voltage-trace spectrum (blue) from the reflections(dotted magenta). For the spectral window the parameters are $r = 0.34$ and $\tau = 3.4\,\mu$s. (For interpretation of the references to colour in this figure legend, the reader is referred to the web version of this article.)

$$|X_{Y-107}(f)| \approx |1 + r\cos(2\pi f\tau)||X_{Dir}(f)|, \quad \text{(A2)}$$

Values for r of ~ 34%, and $\tau \approx 3.4\,\mu s$, can be deduced from Fig. 8(c), and the resulting spectral window is depicted in Fig. 10(b). A suppression of ~ 2.4dB can therefore be inferred for the $f_0/2$ peak of the spectrum detected by Y-107, due to the reflected periodic shock waves.

References

[1] Y. Son, M. Lim, J. Khim, M. Ashokkumar, Acoustic emission spectra and sonochemical activity in a 36 kHz sonoreactor, Ultrason. Sonochem. 19 (1) (2012) 16–21, http://dx.doi.org/10.1016/j.ultsonch.2011.06.001.

[2] M. Ashokkumar, M. Hodnett, B. Zeqiri, F. Grieser, G.J. Price, Acoustic emission spectra from 515 kHz cavitation in aqueous solutions containing surface-active solutes, J. Am. Chem. Soc. 129 (8) (2007) 2250–2258, http://dx.doi.org/10.1021/ja067960r.

[3] I. Tzanakis, M. Hodnett, G.S.B. Lebon, N. Dezhkunov, D.G. Eskin, Calibration and performance assessment of an innovative high-temperature cavitometer, Sens. Actuators, A 240 (2016) 57–69, http://dx.doi.org/10.1016/j.sna.2016.01.024.

[4] A. Sabraoui, C. Inserra, B. Gilles, J.-C. Béra, J.-L. Mestas, Feedback loop process to control acoustic cavitation, Ultrason. Sonochem. 18 (2) (2011) 589–594, http://dx.doi.org/10.1016/j.ultsonch.2010.07.011.

[5] D. Sarno, M. Hodnett, L. Wang, B. Zeqiri, An objective comparison of commercially-available cavitation meters, Ultrason. Sonochem. 34 (2017) 354–364, http://dx.doi.org/10.1016/j.ultsonch.2016.05.024.

[6] J. Lee, S. Kentish, T.J. Matula, M. Ashokkumar, Effect of surfactants on inertial cavitation activity in a pulsed acoustic field, J. Phys. Chem. B 109 (35) (2005) 16860–16865, http://dx.doi.org/10.1021/jp0533271.

[7] J. Frohly, S. Labouret, C. Bruneel, I. Looten-Baquet, R. Torguet, Ultrasonic cavitation monitoring by acoustic noise power measurement, J. Acoust. Soc. Am. 108 (5) (2000) 2012, http://dx.doi.org/10.1121/1.1312360.

[8] V.S. Moholkar, S.P. Sable, A.B. Pandit, Mapping the cavitation intensity in an ultrasonic bath using the acoustic emission, AIChE J. 46 (4) (2000) 684–694, http://dx.doi.org/10.1002/aic.690460404.

[9] B. Zeqiri, M. Hodnett, A.J. Carroll, Studies of a novel sensor for assessing the spatial distribution of cavitation activity within ultrasonic cleaning vessels, Ultrasonics 44 (1) (2006) 73–82, http://dx.doi.org/10.1016/j.ultras.2005.08.004.

[10] K.V. Jenderka, C. Koch, Investigation of spatial distribution of sound field parameters in ultrasound cleaning baths under the influence of cavitation, Ultrasonics 44 (SUPPL.) (2006) 401–406, http://dx.doi.org/10.1016/j.ultras.2006.05.042.

[11] S.Y. Wu, M. Downs, C.S. Sanchez, T. Teichert, A. Buch, G. Samiotaki, F. Marquet, Y.S. Tung, C. Chen, V. Ferrera, E. Konofagou, Monitoring of focused ultrasound-induced blood-brain barrier opening in non-human primates using transcranial cavitation detection in vivo and the primate skull effect, IEEE Int. Ultrason. Symp. IUS (2013) 1201–1204, http://dx.doi.org/10.1109/ULTSYM.2013.0307.

[12] S.Y. Wu, Y.S. Tung, F. Marquet, M. Downs, C. Sanchez, C. Chen, V. Ferrera, E. Konofagou, Transcranial cavitation detection in primates during blood-brain barrier opening-a performance assessment study, IEEE Trans. Ultrason. Ferroelectr. Freq. Control 61 (2014) 966–978, http://dx.doi.org/10.1109/TUFFC.2014.2992.

[13] S.-Y. Wu, C.S. Sanchez, G. Samiotaki, A. Buch, V.P. Ferrera, E.E. Konofagou, Characterizing focused-ultrasound mediated drug delivery to the heterogeneous primate brain in vivo with acoustic monitoring, Sci. Rep. 6 (2016) 37094, http://dx.doi.org/10.1038/srep37094.

[14] M.E. Downs, A. Buch, M.E. Karakatsani, E.E. Konofagou, V.P. Ferrera, Blood-brain barrier opening in behaving non-human primates via focused ultrasound with systemically administered microbubbles, Sci. Rep. 5 (2015) 15076, http://dx.doi.org/10.1038/srep15076.

[15] F. Marquet, T. Teichert, S.Y. Wu, Y.S. Tung, M. Downs, S. Wang, C. Chen, V. Ferrera, E.E. Konofagou, Real-time, transcranial monitoring of safe blood-brain barrier opening in non-human primates, PLoS ONE 9 (2) (2014) 1–11, http://dx.doi.org/10.1371/journal.pone.0084310.

[16] D.M. Hallow, A.D. Mahajan, T.E. McCutchen, M.R. Prausnitz, Measurement and correlation of acoustic cavitation with cellular bioeffects, Ultrasound Med. Biol. 32 (2006) 1111–1122, http://dx.doi.org/10.1016/j.ultrasmedbio.2006.03.008.

[17] E. Lyka, C. Coviello, R. Kozick, C.-C. Coussios, Sum-of-harmonics method for improved narrowband and broadband signal quantification during passive monitoring of ultrasound therapies, J. Acoust. Soc. Am. 140 (1) (2016) 741 URL:http://www.ncbi.nlm.nih.gov/pubmed/27475195.

[18] K. Hynynen, The threshold for thermally significant cavitation in dog's thigh muscle in vivo, Ultrasound Med. Biol. 17 (2) (1991) 157–169, http://dx.doi.org/10.1016/0301-5629(91)90123-E.

[19] E.C. Everbach, I.R.S. Makin, M. Azadniv, R.S. Meltzer, Correlation of ultrasound-induced hemolysis with cavitation detector output in vitro, Ultrasound Med. Biol. 23 (4) (1997) 619–624, http://dx.doi.org/10.1016/S0301-5629(97)00039-2.

[20] Y. Zhou, Reduction of bubble cavitation by modifying the diffraction wave from a lithotripter aperture, J. Endourol. 26 (8) (2012) 1075–1084, http://dx.doi.org/10.1089/end.2011.0671.

[21] J. McLaughlan, I. Rivens, T. Leighton, G. ter Haar, A study of bubble activity generated in ex vivo tissue by high intensity focused ultrasound, Ultrasound Med. Biol. 36 (8) (2010) 1327–1344, http://dx.doi.org/10.1016/j.ultrasmedbio.2010.05.011.

[22] E.A. Brujan, T. Ikeda, Y. Matsumoto, Shock wave emission from a cloud of bubbles, Soft Matter 8 (21) (2012) 5777, http://dx.doi.org/10.1039/c2sm25379h.

[23] C. Desjouy, A. Poizat, B. Gilles, C. Inserra, J.-C. Bera, Control of inertial acoustic cavitation in pulsed sonication using a real-time feedback loop system, J. Acoust. Soc. Am. 134 (2) (2013) 1640–1646 URL:http://www.ncbi.nlm.nih.gov/pubmed/23927204.

[24] C.M. Schoellhammer, A. Schroeder, R. Maa, G.Y. Lauwers, A. Swiston, M. Zervas, R. Barman, A.M. DiCiccio, W.R. Brugge, D.G. Anderson, D. Blankschtein, R. Langer, G. Traverso, Ultrasound-mediated gastrointestinal drug delivery, Sci. Transl. Med. 7 (310) (2015) 310ra168.

[25] C.C. Coussios, C.H. Farny, G. Ter Haar, R.A. Roy, Role of acoustic cavitation in the delivery and monitoring of cancer treatment by high-intensity focused ultrasound (HIFU), Int. J. Hyperthermia 23 (2) (2007) 105–120, http://dx.doi.org/10.1080/02656730701194131.

[26] M.A. Oreilly, K. Hynynen, A PVDF receiver for ultrasound monitoring of transcranial focused ultrasound therapy, IEEE Trans. Biomed. Eng. 57 (9) (2010) 2286–2294, http://dx.doi.org/10.1109/TBME.2010.2050483.

[27] M.A. O'Reilly, K. Hynynen, Blood-brain barrier: real-time feedback-controlled focused ultrasound disruption by using an acoustic emissions-based controller, Radiology 263 (1) (2012) 96–106, http://dx.doi.org/10.1148/radiol.11111417.

[28] M.W. Miller, E.C. Everbach, C. Cox, R.R. Knapp, A.A. Brayman, T.A. Sherman, A comparison of the hemolytic potential of Optison and Albunex in whole human blood in vitro: acoustic pressure, ultrasound frequency, donor and passive cavitation detection considerations, Ultrasound Med. Biol. 27 (5) (2001) 709–721, http://dx.doi.org/10.1016/S0301-5629(01)00356-8.

[29] J.R. McLaughlan, S. Harput, R.H. Abou-Saleh, S.A. Peyman, S. Evans, S. Freear, Characterisation of liposome-loaded microbubble populations for subharmonic imaging, Ultrasound Med. Biol. (2016) 1–11, http://dx.doi.org/10.1016/j.ultrasmedbio.2016.09.011.

[30] A. Lauterborn, Werner Koch, Holographic observation of period-doubled and chaotic bubble oscillations in acoustic cavitation, Phys. Rev. A 35 (4) (1987) 1974–1977.

[31] W. Lauterborn, E. Cramer, Subharmonic route to chaos observed in acoustics, Phys. Rev. Lett. 47 (20) (1981) 1445–1448, http://dx.doi.org/10.1103/PhysRevLett.47.1445.

[32] J.H. Song, K. Johansen, P. Prentice, An analysis of the acoustic cavitation noise spectrum: The role of periodic shock waves, J. Acoust. Soc. Am. 140 (2016) 2494–2505, http://dx.doi.org/10.1121/1.4964633.

[33] J.H. Song, K. Johansen, P. Prentice, J.H. Song, K. Johansen, P. Prentice, Covert cavitation: Spectral peak suppression in the acoustic emissions from spatially configured nucleations, J. Acoust. Soc. Am. 141 (3) (2017) EL216–EL221, http://dx.doi.org/10.1121/1.4977236.

[34] B. Gerold, S. Kotopoulis, C. McDougall, D. McGloin, M. Postema, P. Prentice, Laser-nucleated acoustic cavitation in focused ultrasound, Rev. Sci. Instrum. 82 (4) (2011), http://dx.doi.org/10.1063/1.3579499.

[35] K. Johnston, C. Tapia-Siles, B. Gerold, M. Postema, S. Cochran, A. Cuschieri, P. Prentice, Periodic shock-emission from acoustically driven cavitation clouds: a source of the subharmonic signal, Ultrasonics 54 (8) (2014) 2151–2158.

[36] B. Petit, Y. Bohren, E. Gaud, P. Bussat, M. Arditi, F. Yan, F. Tranquart, E. Allémann, Sonothrombolysis: the contribution of stable and inertial cavitation to clot lysis, Ultrasound Med. Biol. 41 (5) (2015) 1402–1410, http://dx.doi.org/10.1016/j.ultrasmedbio.2014.12.007.

[37] C.C. Church, E.L. Carstensen, Stable inertial cavitation, Ultrasound Med. Biol. 27 (10) (2001) 1435–1437, http://dx.doi.org/10.1016/S0301-5629(01)00441-0.

[38] M. Ashokkumar, The characterization of acoustic cavitation bubbles – an overview, Ultrason. Sonochem. 18 (4) (2011) 864–872, http://dx.doi.org/10.1016/j.ultsonch.2010.11.016.

[39] T.G. Leighton, The Acoustic Bubble, Academic Press, London, 1994.

[40] K. Johansen, J.H. Song, K. Johnston, P. Prentice, Deconvolution of acoustically detected bubble-collapse shock waves, Ultrasonics 73 (2017) 144–153, http://dx.doi.org/10.1016/j.ultras.2016.09.007.

[41] A. Vogel, Shock wave emission and cavitation bubble generation by picosecond and nanosecond optical breakdown in water, J. Acoust. Soc. Am. 100 (1) (1996) 148–165, http://dx.doi.org/10.1121/1.415878.

[42] Datasheet Y-107 and Y-102 Hydrophones, Sonic Concepts, Bothell, WA, USA.

[43] G. Kossoff, The effects of backing and matching on the performance of piezoelectric ceramic transducers, IEEE Trans. Sonics Ultrason. 13 (1) (1966) 20–30, http://dx.doi.org/10.1109/T-SU.1966.29370.

[44] C.S. Desilets, J.D. Fraser, G.S. Kino, The design of efficient broad-band piezoelectric transducers, IEEE Trans. Sonics Ultrason. 25 (3) (1978) 115–125, http://dx.doi.org/10.1109/T-SU.1978.31001.

[45] T.M. Reeder, D.K. Winslow, Characteristics of microwave acoustic transducers for volume wave excitation, IEEE Trans. Microw. Theory Tech. 11 (1969) 927–940.

[46] B. Fay, G. Ludwig, C. Lankjaer, P.A. Lewin, Frequency response of PVDF needle-type hydrophones, Ultrasound Med. Biol. 20 (4) (1994) 361–366, http://dx.doi.org/10.1016/0301-5629(94)90004-3.

[47] T.L. Szabo, Diagnostic Ultrasound Imaging: Inside Out, Academic Press, 2004.

[48] L.E. Kinsler, A.R. Frey, A.B. Coppens, J.V. Sanders, Fundamentals of Aoustics, Wiley-VCH, 1999.